Morphological and optical transitions during micelle-seeded chiral growth on gold nanorods

Morphological and Optical Transitions during Micelle-Seeded Chiral Growth on Gold Nanorods

Xiaolu Zhuo[1,2,*,**], *Mikhail Mychinko*[3], *Wouter Heyvaert*[3], *David Larios*[4], *Manuel Obelleiro-Liz*[5], *José M. Taboada*[4], *Sara Bals*[3] *and Luis M. Liz-Marzán*[1,2,6,*]

[1] CIC biomaGUNE, Basque Research and Technology Alliance (BRTA), Paseo de Miramón 182, 20014 Donostia-San Sebastián, Spain

[2] Centro de Investigación Biomédica en Red de Bioingeniería, Biomateriales y Nanomedicina (CIBER-BBN), Paseo de Miramón 182, 20014 Donostia-San Sebastián, Spain

[3] Electron Microscopy for Materials Research (EMAT) and NANOlab Centre of Excellence, University of Antwerp, 2020 Antwerp, Belgium

[4] Departamento de Tecnología de los Computadores y de las Comunicaciones, University of Extremadura, 10003 Cáceres, Spain

[5] EM3 Works, Spin-off of the University of Vigo and the University of Extremadura, PTL Valladares, 36315 Vigo, Spain

[6] Ikerbasque, Basque Foundation for Science, 48013 Bilbao, Spain

[*] Corresponding authors email: zhuoxiaolu@cuhk.edu.cn (X.Z.); llizmarzan@cicbiomagune.es (L.M.L.-M.)

** Current address: School of Science Engineering, The Chinese University of Hong Kong (Shenzhen), Shenzhen 518172, China

ABSTRACT: Chiral plasmonics is a rapidly developing field where breakthroughs and unsolved problems coexist. We have recently reported a binary surfactant-assisted seeded growth of chiral gold nanorods (Au NRs) with high chiroptical activity. Such a seeded-growth process involves the use of a chiral co-surfactant that induces micellar helicity, in turn driving the transition from achiral to chiral Au NRs, both from the morphological and from the optical points of view. We report herein a detailed study on both transitions, which reveals intermediate states that were hidden so far. The correlation between structure and optical response is carefully analyzed, including the (linear and CD) spectral evolution over time, electron tomography, the impact of NR dimensions on their optical response, the variation of absorption-to-scattering ratio during the evolution from achiral to chiral Au NRs, and the near-field enhancement related to chiral plasmon modes. Our findings provide further understanding on the growth process of chiral Au NRs and the associated optical changes, which will facilitate further study and applications of chiral nanomaterials.

KEYWORDS: chirality; chiral plasmonics; seeded growth; circular dichroism; electron tomography.

INTRODUCTION

Intrinsically chiral plasmonic nanostructures support localized surface plasmon resonances (LSPRs) that respond differently to left- and right-handed circularly polarized light, while displaying the usual characteristics of LSPRs, such as local field enhancement, antenna effect, hot-carrier production, and photothermal effects.[1,2] A combination of chirality and conventional plasmonic features creates opportunities for the design of more efficient nanophotonic and optoelectronic devices,[3–5] biosensing and biomedical applications,[6–8] photochemistry,[9] and surface-enhanced spectroscopies.[10] Therefore, plasmonic nanostructures with strong chiroptical activity are ideal platforms for studying such phenomena and applications.

The fabrication of 2D or 3D chiral plasmonic nanostructures with strong chiroptical activity and high throughput has been reported by means of both top-down and bottom-up methods.[11–14] Although top-down lithography techniques have demonstrated a wide versatility and high precision, bottom-up approaches usually show advantages related to large-scale production, straightforward surface functionalization, and flexibility toward their use in both solution-based and solid-state-based applications.[15,16] Until recently, most of the bottom-up methods have relied on the so-called template-assisted self-assembly, where RNA,[17] DNA,[18] proteins,[7] liquid crystals,[19,20] or other scaffolds with helical structures were used as templates to drive the organization of achiral plasmonic nanoparticles into chiral plasmonic assemblies.[21]

The colloidal synthesis of intrinsically chiral plasmonic nanoparticles has recently emerged as a promising alternative for the preparation of 3D chiral structures with high optical activity.[16] These synthetic methods typically rely on using chiral molecules or chiral co-surfactants to impart chirality into the nanoparticle morphology during growth. Such a process is more challenging than it sounds, as indicated by the few examples that have been reported so far. Nam and co-workers

demonstrated seeded chiral growth of Au nanocubes into helicoids with intricate twisted morphologies and strong chiroptical signals (g-factor ~0.2), using amino acids and peptides as the shape-directing agents, which were proposed to induce atomic scale chirality.[13] As an extension of this strategy, the same group conducted detailed studies on other types of Au helicoids with further control over the morphology and chiroptical response.[22–26] An alternative strategy was reported by our groups, which relied on the use of chiral co-surfactants to obtain quasi-helical micelles that would in turn serve as templates for the seed-mediated growth of chiral Au nanorods (NRs). It should be noted that the morphological features leading to chirality are significantly different in this case, comprising helical wrinkles all around the Au NR surface, and leading to high optical activities over a wide wavelength range, with g-factors reaching 0.25.[14] More recently, Sun *et al.* demonstrated the production of chiral Au nanoplates with record high g-factor reaching 0.44, using cysteine-phenylalanine as shape-directing chiral molecules deposited on Au nanoprism seeds.[8,27] Although the toolkit of intrinsically chiral plasmonic nanoparticles is thus becoming more diverse and leading to improved chiroptical performance, there is still a knowledge gap regarding the growth mechanisms of chiral nanostructures and their connection with the recorded optical features.

We have therefore carried out a systematic study toward better understanding the micelle-directed seeded growth, from achiral single-crystal Au NRs into chiral Au NRs (rod-shaped structures with helical wrinkles). We made extensive use of electron microscopy and electron tomography, to reveal the morphological and crystallographic evolution during chiral growth on Au NRs. We additionally monitored the optical response during chiral growth, through both time-dependent and steady-state UV-visible-near IR (UV-vis-NIR) and circular dichroism (CD) spectral measurements. To properly distinguish the contributions of absorption and scattering to the overall

optical response, an integrating sphere was used, which revealed an unusual size-dependent evolution, compared to that of conventional plasmonic nanoparticles. We further carried out numerical simulations to understand the physical origin of chiral plasmon modes and the observed absorption-to-scattering ratios.

RESULTS AND DISCUSSION

The growth of chiral plasmonic objects can be in principle correlated to the observation of optical activity within the vis-NIR range. Therefore, time-dependent extinction and CD measurements can be used to monitor *in situ* any spectral changes occurring during the transition from achiral to chiral Au NRs, as reported in **Figure 1**. We initially relied on the optimized growth conditions reported in ref. 14. The starting Au NRs were prepared according to a previously reported seeded growth method, using cetyltrimethylammonium bromide (CTAB) and *n*-decanol as binary surfactants.[28] The obtained Au NRs are achiral, single-crystalline, and highly monodisperse, with the usual (rounded) octagonal cross-section and rounded tips (**Figure 1A**). For this experiment, the average length and diameter were 112 ± 10 nm and 15 ± 1 nm, respectively. The as-prepared Au NRs were carefully washed and subsequently incubated in an aqueous solution of cetyltrimethylammonium chloride (CTAC, 25 mM) and 1,1'-binaphthyl-2,2'-diamine (BINAMINE, 0.625 mM). We propose that incubation of Au NRs with the BINAMINE-CTAC surfactant mixture leads to the adsorption of worm-like micelles with axial chirality around the NR lateral surface. These NRs were then used as seeds in an additional step of surfactant-assisted seeded growth, to produce chiral Au NRs, as described in our previous work.[14] In the presence of the micellar template, additional reduction of Au atoms should follow the quasi-helical morphology of the worm-like micelles, giving rise to larger Au NRs with wrinkles on their surface (**Figure 1B**), which resemble the

structures that were previously shown to be quasi-helical by three-dimensional (3D) electron tomography reconstructions and fast Fourier transformations.[14] Under these conditions and with the relatively high concentration of reducing agent (ascorbic acid, ~0.16 M) used to induce seeded-growth, the achiral-to-chiral transition was found to be completed within 10 minutes, as revealed by the temporal evolution of both extinction and CD spectra (**Figures 1C,D and S1**). For completeness, both (*R*)- and (*S*)-BINAMINE enantiomers were used as co-surfactants in the templating micelles, which indeed resulted in the formation of chiral Au NRs with opposite handedness (specular features in the CD spectra). In both cases, the real-time extinction spectra revealed a longitudinal LSPR band gradually shifting from above 1100 nm toward 900 nm during the first 1 minute, but then fading away. After complete damping of the longitudinal LSPR band, only an extinction band remains around 550 nm, which is usually associated to a transverse LSPR mode in Au NRs. Both this band and a long tail toward longer wavelengths keep increasing in intensity, which is likely related to a gradual increase in particle size during chiral overgrowth. Although the final products retain an overall rod-like shape, it is worth noting that the longitudinal LSPR band seems to disappear after the achiral-to-chiral transition, which will be further discussed below. Although the growth of (*R*)- and (*S*)-type chiral Au NRs appears to be basically identical from the perspective of real-time extinction spectra, circular dichroism (and the corresponding g-factor) spectra (**Figures 1C, S1**) exhibit CD bands with opposite signs and high symmetry, likely arising from the formation of Au wrinkles coiling in opposite directions on the surface of chiral Au NRs. It is interesting to note that, in both cases, three CD bands are appreciated after the first minute of the reaction, followed by a gradual red-shift and increase in chiroptical intensity until a steady state is eventually reached. It thus appears that a crucial event is needed to start the achiral-to-chiral transition, which in this case occurs around minute 1 of the seeded-growth reaction.

However, due to the fast reaction rate, it is challenging to monitor the growth process by detaining the reaction instantaneously at different stages and studying the corresponding morphological changes.

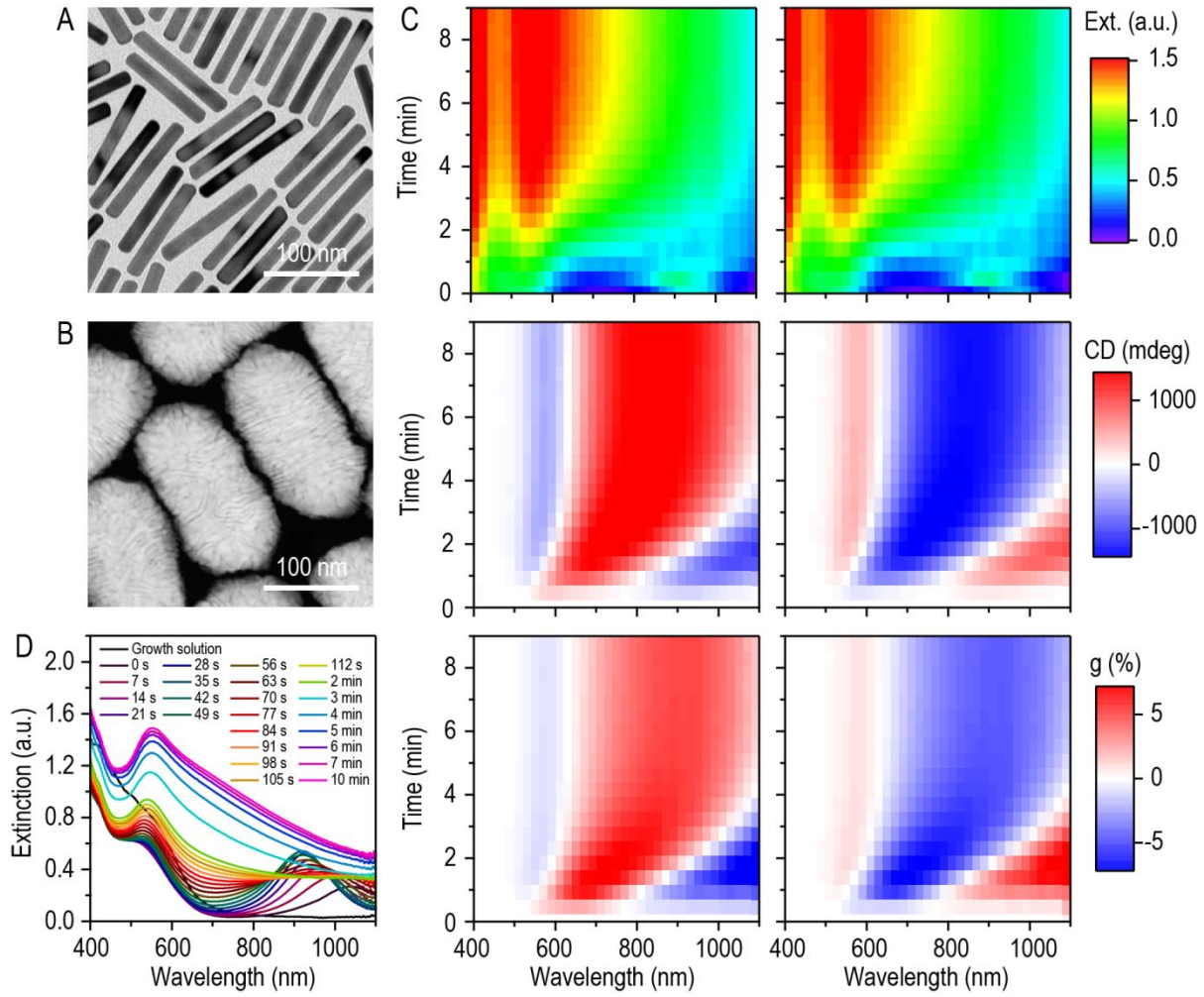

Figure 1. Growth of chiral Au NRs. (A) TEM image of single-crystalline Au NRs (length, 112 ± 10 nm; diameter, 15 ± 1 nm) used as seeds for chiral overgrowth. (B) Representative HAADF-STEM image of the resulting chiral Au NRs (length, 193 ± 11 nm; diameter, 106 ± 4 nm). (C) Time-dependent extinction (upper panel), circular dichroism (middle panel), and g-factor (bottom panel) spectra of chiral Au NRs during the first 10 minutes of the overgrowth process, using (*R*)-

BINAMINE-CTAC (left-hand column) and (*S*)-BINAMINE-CTAC (right-hand column) surfactant mixtures. (D) Time-dependent extinction spectra with smaller time steps, using (*R*)-BINAMINE-CTAC surfactant mixture in the chiral overgrowth (see also **Figure S1** for time-dependent CD and g-factor spectra with both enantiomers).

Therefore, we used an alternative method to mimic the reaction progress around minute 1, by carrying out a series of syntheses in which we varied the seed concentration for chiral overgrowth, let the reaction proceed to a steady state, and analyzed the spectral and morphological features of the obtained products (**Figures 2, S2, and S3**). Assuming an equivalent growth mechanism for (*R)*- and (*S)*-type chiral Au NRs,[14] we focus in what follows on *R*-type NRs for simplicity. The seed concentration is defined through the $[Au^0]/[Au^+]$ ratio, between the achiral Au NR seed solution ($[Au^0]$, *i.e.*, Au atom concentration) and the chiral overgrowth solution ($[Au^+]$, *i.e.* $[Au^{+3}]$ after partial reduction by ascorbic acid). When low seed concentrations were used, a relatively high amount of Au^+ ions were available for overgrowth onto each achiral Au NR, thus leading to the formation of helical wrinkles and chiral Au NRs, similar to those shown in **Figure 1B**. When the seed concentration was increased, the relative amount of Au^+ ions that could be reduced onto each Au NR would decrease accordingly. At the highest seed concentrations, Au^+ ions in the growth solution might be depleted even prior to the formation of wrinkles, which we expect to mimic the initial stages of the achiral-to-chiral transition.

To investigate the intricate morphological evolution expected for this process, the different samples were analyzed by electron tomography based on high-angle annular dark-field scanning transmission electron microscopy (HAADF-STEM) (see Methods). We applied this technique to the achiral Au NR seeds and representative Au NRs overgrown at different $[Au^0]/[Au^+]$ ratios, to

reconstruct their 3D morphologies (**Figure 2A–D** and **Supplementary Movies S1-S12**). As shown in **Figure 2A**, the seeding Au NRs are single-crystalline with a rounded octagonal cross-section, which has been reported to comprise alternating {100}, {520} and {110} facets.[29] Upon overgrowth with an $[Au^0]/[Au^+]$ ratio of 0.31 (**Figures 2B** and **S4**), we observed a transition into a four-fold symmetric shape with square cross-section and pyramidal tips, *i.e.*, an elongated octahedral shape. According to previous studies, four-fold symmetric Au NRs may exist as different geometrically allowed structures, comprising lateral sides enclosed by {100}, {110}, or {111} facets.[30–32] We carried out electron diffraction measurements along different directions, which revealed four lateral {110} facets (**Figure S4A**). According to the 3D reconstruction and orthoslices, the square cross-section shows a rotation of 45° from one end to the center along the Au NR longitudinal axis (**Figure S4B**). Moreover, the angle between an end facet and a lateral edge was measured to be 135°, whereas the tip angle at different views was measured as either 109° or 90° (**Figure S4C**), all of which are characteristic angles of fcc crystals with adjacent {110} facets. Combined together, we can conclude that the four-fold symmetric Au NR is enclosed by twelve {110} facets, including the four lateral sides and four smaller facets at each end (**Figure S4D**). It is also worth noting that all facets are slightly concave, which likely indicates a precursor state to the subsequently emerging wrinkles. When the seed concentration ($[Au^0]/[Au^+]$ ratio) was reduced to 0.13, the obtained Au NRs already displayed helical wrinkles on the surface, albeit short and rather disordered (**Figure 2C**). Well-defined chiral Au NRs with rich helical wrinkles were obtained with a significantly lower $[Au^0]/[Au^+]$ ratio of 0.03 (**Figure 2D**). Interestingly, both of the orthoslices in Figures 2C and 2D also display a quasi-square cross-section, similar to that in Figure 2B, but with additional protrusions at edges and corners. With the aim of better understanding the morphology of the different samples, we applied a recently developed

methodology to quantify the helical morphology of NRs, which is based on the analysis of 3D tomography reconstructions.[33] Our results indicate an increase in left-handed total helicity during the gradual formation of helical wrinkles (**Figure S5**). Although both left- and right-handed local helical features can be recognized in all of the overgrown Au NRs, the relative amount of left-handed features increases as helical wrinkles are more clearly distinguished, in agreement with an achiral-to-chiral transition. It is interesting to note that the inclination angles of early-stage helical wrinkles (75°–90°, **Figure S5A,B**) are steeper than those for well-defined helical structures (<45°, **Figure S5C**). This is in agreement with our earlier observation that the inclination angles of helical wrinkles depend on the thickness of the helical shell.[33]

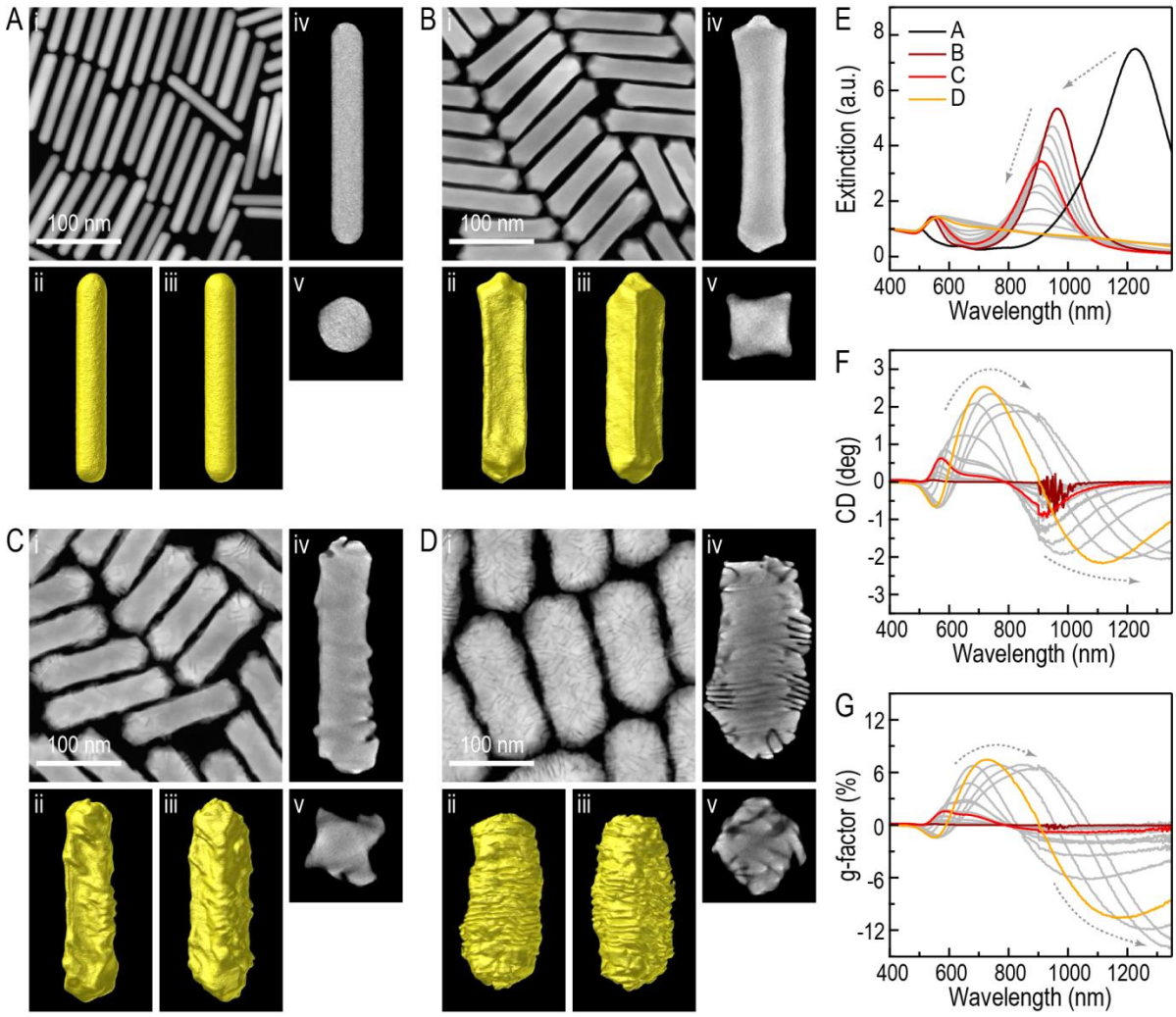

Figure 2. Morphological and spectral characterization of Au NRs obtained by varying seed concentration in chiral overgrowth. (A) HAADF-STEM image, tomography reconstruction and selected orthoslices of single-crystalline seed Au NRs. (B–D) Morphology of Au NRs grown with decreasing seed concentration, *i.e.*, decreasing $[Au^0]/[Au^+]$ ratio between seed and growth solution (B: 0.31; C: 0.13; D: 0.03). The morphological characterization for each sample includes (i) HAADF-STEM image, (ii,iii) 3D reconstructions along different viewing angles, (iv,v) selected orthoslices perpendicular to the longitudinal and transverse axes at the center of the NRs. Animated 3D reconstructions and orthoslices are provided as **Supplementary Movies S1-S12**. (E-G) Extinction (E), CD (F), and g-factor (G) spectra of samples prepared with varying seed NR concentrations. The colored curves correspond to the 4 samples shown in (A–D). Dashed arrows indicate increasing chiral shell thickness, corresponding to decreasing concentration of Au NR seeds in the syntheses. Extinction spectra were normalized to the absorbance at 400 nm (OD_{400} = 1). CD spectra were scaled equally, according to the corresponding extinction spectra.

The spectral evolution of this series of synthetic samples (**Figure 2E–G, S3**) also resembles closely the one measured during an extended synthesis (**Figure 1C,D**), including a gradual blue-shift and eventual disappearance of the longitudinal LSPR band as the chiral morphology becomes more pronounced (lower seed concentration), a red-shift and increasing intensity of all bands in the CD spectra, as well as a highest g-factor of the positive CD band at 700–800 nm (higher g-factors were recorded further into the NIR, in agreement with our previous report).[14] When comparing the data between Figures 1 and 2, it should be noted that, in Figure 1C,D, the spectra were directly measured from the growth solutions, *i.e.*, the particle concentration was constant in each reaction step, whereas the concentration of reduced Au atoms increased with time. In **Figure 2E**,**F**, it was challenging to normalize the spectra of different samples to a fixed particle

concentration, and thus extinction spectra were normalized to the intensity at 400 nm, as an approximation to a fixed total Au^0 concentration. Each CD spectrum was accordingly adjusted in equal proportion to the intensity change of the corresponding extinction spectrum. The g-factor spectra (**Figure 2G**) are independent, by definition, of both particle concentration and Au concentration and can thus be compared directly to those in **Figure 1C**. Overall, despite some differences in peak intensities, the spectral evolution in **Figure 2E–G** agrees well with those shown in **Figure 1**, thereby confirming the feasibility of this approach to mimic the different stages during chiral overgrowth, and allowing for a case-by-case comparison between morphological and spectral changes. As shown in **Figure S2**, both the length and diameter of Au NRs increase during chiral overgrowth, resulting in an overall decrease in aspect ratio (length-to-diameter ratio), in agreement with the initial blue-shift of the longitudinal plasmon band as the seed concentration decreases. The reason behind the broadening and eventual disappearance of the longitudinal plasmon band is less obvious, we propose that it is related to a combined effect: (i) the decay of charge oscillations within helical wrinkles, which become well-defined at an $[Au^0]/[Au^+]$ ratio lower than 0.13 (**Figure 2C**); and (ii) broader size and shape distributions after overgrowth.

Assuming that this analysis reflects the behavior during direct chiral overgrowth, we propose the existence of two main stages: first, preferential Au deposition on high-index {520} facets until the formation of slightly twisted elongated octahedra, followed by the formation of helical wrinkles, which are likely directed by adsorbed BINAMINE-CTAC micelles. We therefore attempted to artificially separate both stages by using the elongated octahedra as seeds in a separate chiral overgrowth reaction, where helical wrinkles would be formed directly on the quasi-square lateral sides, producing helical Au NRs with chiroptical response (**Figure S6**). We again observed a flattening of the longitudinal plasmon band and a continuous red-shift of CD bands, similar to

those shown in Figures 1 and 2. Relatively low g-factors were obtained in this case, likely due to the multiple cleaning steps involved in this process, which would hinder the alignment of BINAMINE-CTAC micelles. These results suggest that the formation of a quasi-square cross-section may play a crucial role in the achiral-to-chiral transition of Au NRs.

As an additional evidence to verify this point, we prepared achiral Au NRs with a quasi-square cross-section, according to a previously reported method.[34] Such Au quasi-cuboids (QCBs) were reported to display well-defined {100} facets, which could be coated by a thin layer of Pd (**Figures 3A,B** and **S7A,B**). The synthesized Au@Pd QCBs were used as seeds under the conditions previously identified to generate chiral Au NRs, *i.e.* following the same incubation and chiral overgrowth procedures. It should be noted that Au QCBs were prepared in the absence of any chiral molecules that might influence the early growth transition. As a result, chiral wrinkles were grown on non-chiral Au QCB, which also displayed chiroptical response (**Figure 3C,D**). Although the g-factors of these samples are relatively low, which may be related to the presence of the Pd intermediate layer and less uniform wrinkles, the overall profile and variation trend of the CD bands are similar to those described above. Most interestingly, the Pd layer can be used to identify the boundary between the achiral QCB cores and the chiral features in the final Au NRs (**Figure 3E**).[35] The thin Pd layer can be distinguished from the contrast difference in the orthoslices of the HAADF-STEM tomography reconstruction (**Figure 3E, iii and iv** and **Figure S7C,D**), showing that helical wrinkles can grow directly on the Pd-covered surface of achiral QCBs, and thereby confirming the role of the quasi-square intermediate morphology in the achiral-to-chiral transition. It should be noted that, although both these QCBs and the elongated octahedra identified as intermediates display a quasi-square cross-section, their structure differs in the crystallographic index of their facets ({100} *vs.* {110}) and their tip morphologies (flat *vs.* pointed). We therefore

conclude that the crystalline nature of lateral facets does not play a major role in chiral growth, again supporting the micelle-templating hypothesis.

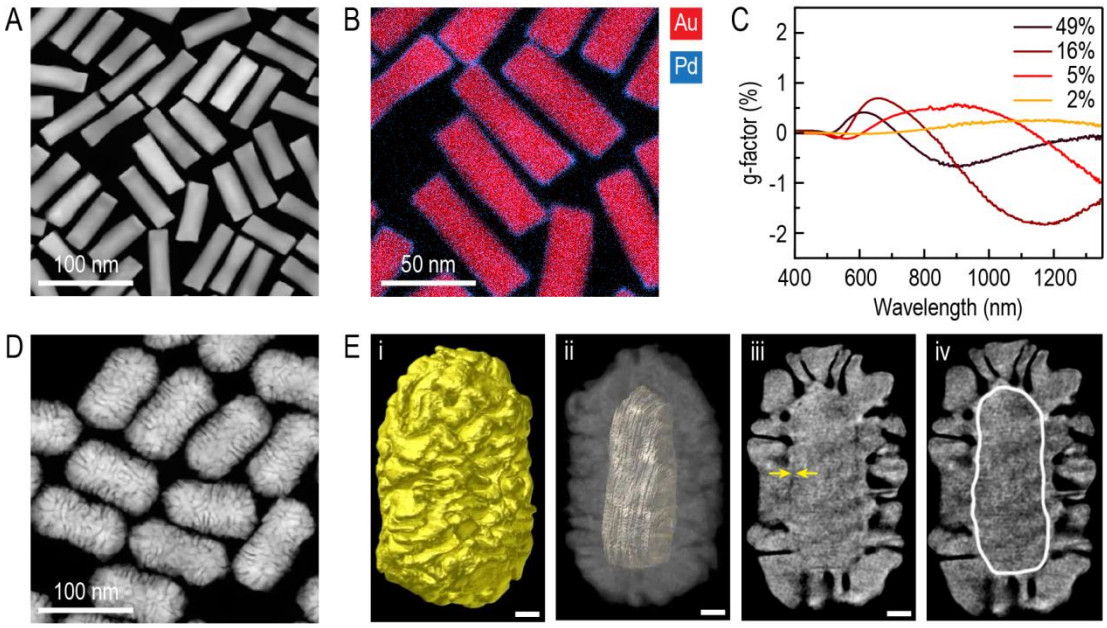

Figure 3. Chiral overgrowth using Au@Pd quasi-cuboids (QCBs) as seeds. (A) HAADF-STEM image of Au@Pd QCBs (length: 66 ± 5 nm; diameter: 22 ± 2 nm). (B) Elemental mapping of Au@Pd QCBs (red, Au; blue, Pd) showing a Pd thin layer coating the surface of Au QCBs. (C) g-factor spectra of chiral Au NRs using different concentrations of QCB seeds. (D) HAADF-STEM image of the QCB-directed chiral Au NRs ($[Au^0]/[Au^+] = 0.16$). (E) Tomography reconstruction of a QCB-seeded chiral Au NR. (i) 3D visualization of the external Au surface; (ii) 3D visualization of the Pd-Au interface; (iii,iv) Orthoslice perpendicular to the transverse axis, where the Pd layer can be seen as a thin, darker line surrounding the core, as indicated by the yellow arrows in (iii) and white outline in (iv). Scale bars: 10 nm. An orthoslice perpendicular to the longitudinal axis of the QCB-directed chiral Au NR is shown in **Figure S7C,D**. See also **Supplementary Movies S13-S15**.

We additionally studied the effect of seed dimensions on the chiroptical activity, specifically focusing on the g-factor. Two series of Au NR samples were prepared for comparison:[28] a first series with a fixed average diameter of ~30 nm and aspect ratios ranging from 2.7 to 5.0 (**Figure 4A–C**); a second series with a smaller diameter of ~15 nm and aspect ratios ranging from 3.1 to 7.5 (**Figure 4D–F**). We therefore covered a wide range of linear LSPR wavelengths, dictated by the varied aspect ratios (**Figure 4G**). Each of these Au NR samples was incubated in (*R*)-BINAMINE-CTAC solution and then a set of chiral overgrowth experiments were carried out by varying Au NR seed concentration. Regardless of the seed dimensions, the achiral-to-chiral transition was invariably found to follow the same morphological and spectral trends as those described in **Figures 2** and **S8–S10**. However, the aspect ratio of the seed Au NRs has a significant impact on both the peak positions and the intensities of the measured CD bands. The g-factor of the positive CD band was observed to achieve a maximum value at a certain optimal seed concentration, regardless of seed dimensions, as labeled with pink bars in **Figure 4A–F**. The chiral Au NR samples corresponding to the maximum g-factor were thus identified as the optimal samples of each series. For each optimal sample, we plotted the wavelength of positive CD band against the average aspect ratio of corresponding Au NR seeds (**Figure 4H**). Interestingly, there is a scaling relationship between the CD band wavelength and the seed aspect ratio. Similarly, we plotted the g-factors ($|g_{max}|$) of the positive and negative CD bands *vs.* the average aspect ratio of the Au NR seeds (**Figure 4I**), showing that Au NR seeds with higher aspect ratios consistently yielded chiral Au NRs with higher g-factors. Notably, the seed concentrations used for producing optimal samples are ~8% for the thicker seeding Au NRs (d_{seed} ~30 nm) and ~3% for the thinner ones (d_{seed} ~15 nm), regardless of their aspect ratio (**Figure S11**). Although we do not have at

present clear evidence of why the aspect ratio and seed concentration play such important roles, we propose that this may be related to the organization of helical micelles around the Au NR seeds. These results provide useful hints for the preparation of chiral Au NRs with different sizes, CD band wavelengths, and g-factors.

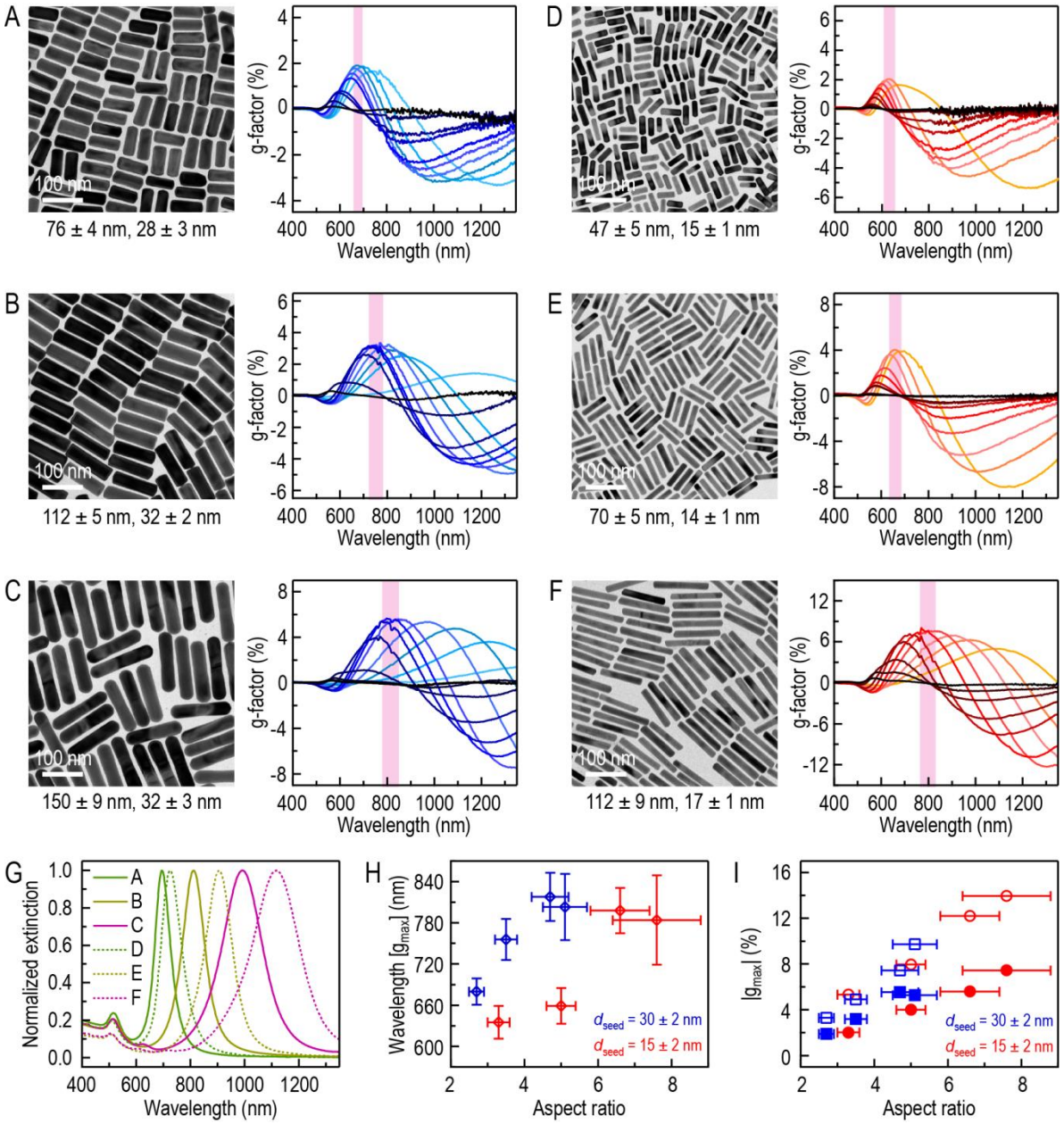

Figure 4. Effect of seed dimensions on g-factor. (A–F) TEM images of Au NR seeds with different sizes (left-hand panels) and g-factor spectra of the resulting chiral NRs (right-hand panels). The average lengths and diameters of the Au NR seeds are indicated below each TEM image. The samples are sorted into two sets with different diameters (blue, d_{seed} = 30 ± 2 nm; red, d_{seed} = 15 ± 2 nm). The trend from darker to lighter colors represent chiral Au NRs with increasing chiral shell thickness. The positive CD band with maximum g-factor is labeled by a pink bar, as a guide to the eye. All chiral Au NRs were grown in the presence of (*R*)-BINAMINE-CTAC surfactant mixtures. (G) Normalized extinction spectra of the Au NR seed samples in (A–F). (H) Peak wavelength of the positive CD band with maximum g-factor *vs.* average aspect ratio of Au NR seeds. (I) Dependence of maximum g-factor on the average aspect ratio of Au NR seeds. Solid and hollow dots correspond to positive and negative CD bands, respectively.

When trying to understand the origin of optical activity in plasmonic nanostructures, it has been common practice (as we have done above) to evaluate the circular dichroism and corresponding g-factor in terms of extinction, *i.e.,* the combined effects of absorption and scattering of light by the plasmonic nanoparticles. However, absorption and scattering have different origins and play different roles in significant plasmonic phenomena and applications. For example, plasmonic NPs with high absorption are usually employed as light absorbers and heaters, whereas those with a high scattering component are more promising for imaging and color display.[36] Therefore, it is essential to distinguish their relative contributions to plasmonic extinction. The absorption-to-scattering ratio is considered to be an important figure of merit.[36] In this context, we selected one of our series of chiral Au NRs to investigate the contributions of scattering and absorption to their extinction spectra, as well as the corresponding trend during the achiral-to-chiral transition. We

measured Au NRs dispersed in water, using a UV-vis-NIR spectrometer equipped with an integrating sphere, where absorption and diffuse reflectance can be recorded with and without a standard diffuse reflector mounted at the transmission port, respectively (**Figure 5A,B**). The absorption, scattering, and extinction spectra can be subsequently calculated according to a previously reported protocol.[37] As a general rule, the extinction of large nanoparticles is known to be dominated by scattering because the absorption cross-section scales with a^3, whereas the scattering cross-section scales with a^6, where a represents the nanoparticle radius.[38]

Our Au NR seeds with relatively large sizes of (150 ± 9 nm) × (32 ± 3 nm), exhibit almost equal scattering and absorption intensities near the longitudinal plasmon band, whereas absorption is dominant around the transverse plasmon band (**Figures 5C, S12**). Shown in **Figure 5D** are the spectra of overgrown Au NRs with elongated octahedral shape and dimensions of (188 ± 10 nm) × (50 ± 2 nm), for which the contribution of scattering is found to increase throughout the whole spectral range, as expected for a significant increase in particle size. However, as the overgrown shells on Au NRs become more wrinkled, despite the additional increase in particle size, we recorded higher contributions of absorption compared to scattering, especially at longer wavelengths (**Figures 5E,F, S12**). We calculated the absorption/scattering ratios for these Au NRs by integrating the spectral intensities in two regions (**Figure 5G**), 500–700 nm and 700–1300 nm, which would correspond to the transverse and longitudinal plasmon bands, respectively. The *x*-axis in **Figure 5G**, from left to right, denotes increasing Au NR sizes. On one hand, the blue curve, corresponding to the result from integrating at the 500–700 nm wavelength range, shows a decreasing absorption/scattering ratio for increasing particle size, in agreement with the general rule that larger plasmonic nanoparticles display greater scattering. On the other hand, the red curve corresponding to the 700–1300 nm wavelength range displays a maximum absorption/scattering

ratio, at which absorption is 2–3 times higher than scattering, which is unusual for plasmonic nanoparticles with such large dimensions above 200 nm (**Figure S13**). For comparison, we simulated the absorption, scattering, and extinction spectra of conventional Au NRs (spherocylinders) by setting the same sizes as those in our experimental chiral Au NR samples.[39] As shown in **Figure S14**, the simulated spectra are dominated by scattering, except for the two smallest models, in good agreement with our experimental results measured from achiral Au NRs. The absorption/scattering ratios of these simulation models are close to zero in both wavelength regions (**Figure S15**). The abnormally high absorption by chiral Au NRs is therefore expected to be related to the chiral wrinkled features because the most intense CD bands are located within the integrating wavelength range at 700–1300 nm, as shown by a color map in **Figure 5G**.

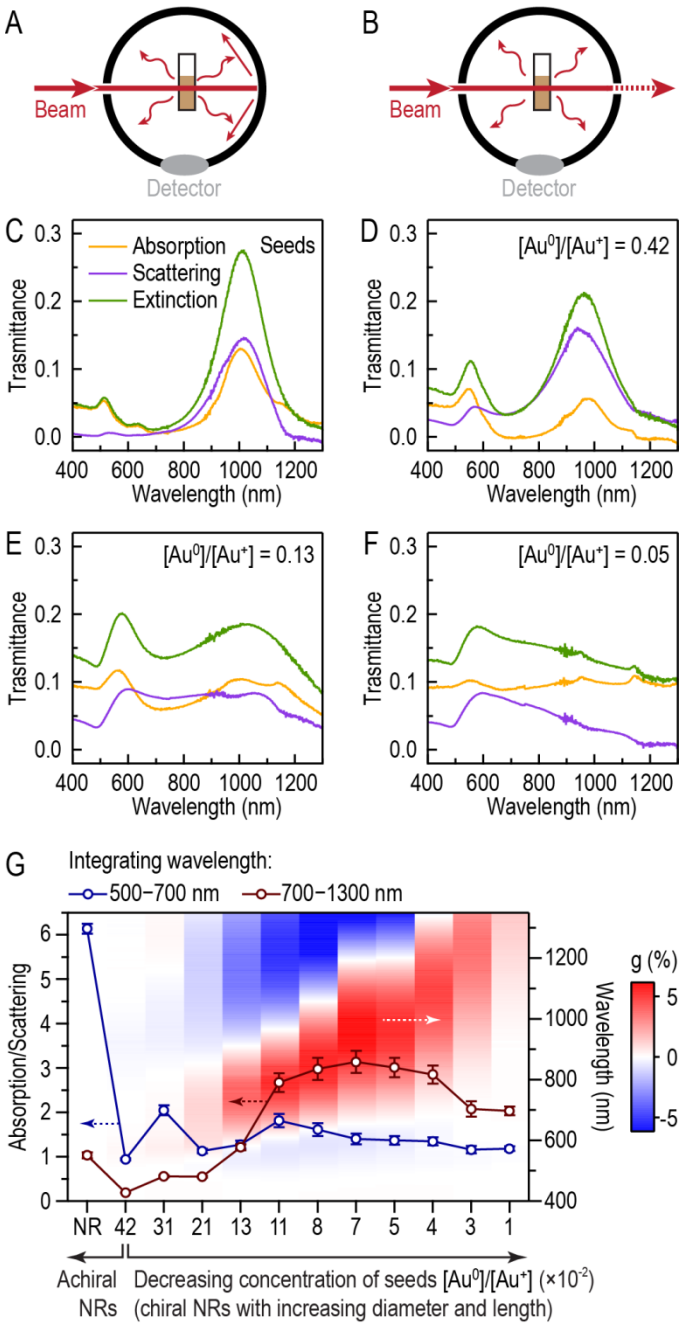

Figure 5. Diffuse reflectance UV-vis-NIR spectroscopy. (A) Schematic illustration of the integrating sphere with a standard diffuse reflector mounted at the transmission port. A cuvette containing the nanoparticle colloid is positioned at the center of the integrating sphere. The detected signal is a sum of scattered and transmitted light. (B) Schematic illustration of the integrating sphere with a light trap to absorb all of the transmitted light, so only scattered light can

reach the detector. (C–F) Representative spectra showing the absorption and scattering contributions to total extinction for Au NR seeds (C) and overgrown Au NRs using different $[Au^0]/[Au^+]$ ratios (D: 0.42; E: 0.13; F: 0.05). (G) Absorption-to-scattering ratios measured from different samples. In both integration wavelength regions (blue: 500–700 nm; red: 700–1300 nm), the measured signals were summed up to calculate the total absorption, total scattering, and therefrom the absorption-to-scattering ratio. The *x*-axis, from left to right, represents an overall increase in nanoparticle size, both in diameter and length. The numbers in the *x*-axis denote the $[Au^0]/[Au^+]$ ratios used in the syntheses. The underlying color map represents the g-factor spectra measured from these samples, corresponding to the *y*-axis and color scale bar on the right.

Finally, we carried out electromagnetic simulations (see details in Methods), to further understand the origin of chiral plasmon modes and the abnormally high absorption of chiral Au NRs. We applied a 3D computer-aided design model by creating helical grooves carved on a larger rod. Even though this model may seem too perfect as compared to our irregular chiral Au NRs, it was previously shown appropriate to confirm the optical activity of chiral Au NRs.[14] Indeed, the simulation results do not coincide perfectly with our experimental spectra, as can be seen in **Figure 6A**, where both the longitudinal and transverse plasmon bands are visible in the simulated spectra (these differences can be attributed to the different morphology and the lack of polydispersity of the simulated NRs with respect to the real sample). It should be noted that, in both cases, absorption clearly dominates over scattering at the longitudinal plasmon band, whereas at the transverse plasmon band absorption and scattering show similar intensities, which is consistent with our experimental measurements. The chiroptical response is calculated from the difference in intensities of optical cross-sections under quasi-axial left-handed circularly polarized (LHCP) and

right-handed circularly polarized (RHCP) excitation (**Figure 7**), and under transversal LHCP and RHCP excitation (**Figure S16**), all of which exhibit local field enhancement inside the helical grooves, especially those under transversal excitation at 1475 nm (**Figure S16C**). Such strong charge oscillations near these tiny structures generate a great amount of heat losses, leading to high absorption of light. In other words, although the overall size of the chiral Au NR is relatively large, the abundance of tiny structural features appears to be the key to enhanced light absorption. To shield the impact of chirality, we also calculated the optical cross-sections of Au NRs of the same dimensions but with parallel wrinkles, which are thus achiral. The results confirmed that the high absorption of light indeed originates from the outer structural features (**Figure S17**). We additionally observed that the near-field response differs significantly for both polarizations, especially at 725 nm (within the band of highest CD), revealing that the origin of the strong plasmonic chiroptical activity is associated with the pattern of sharp wrinkles and grooves on the NR surface. The response is higher under LHCP excitation, which correlates well with the positive CD values.

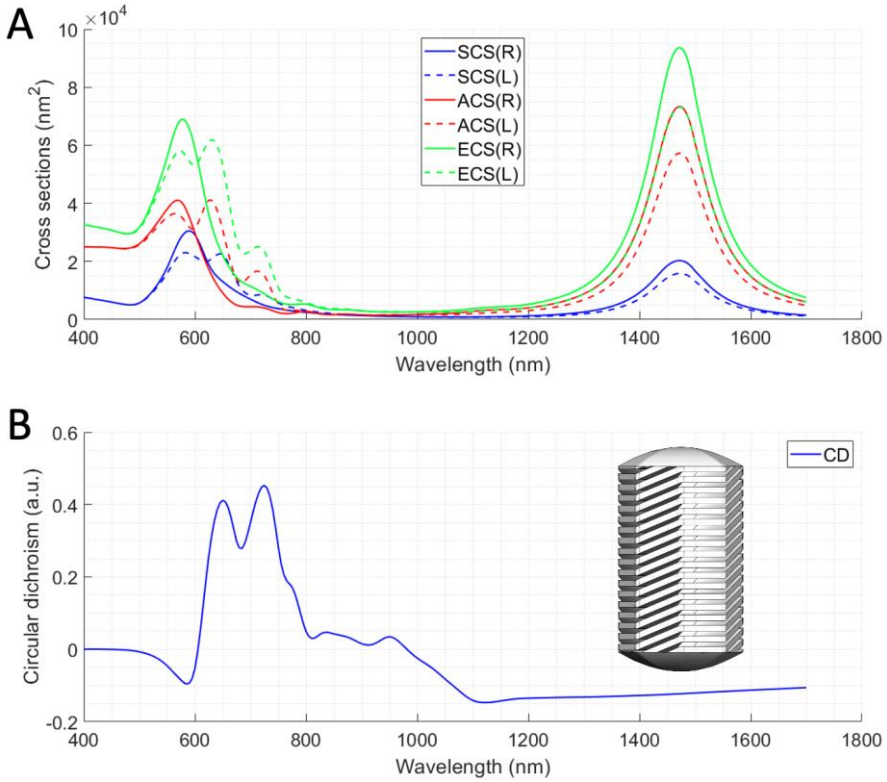

Figure 6. Simulations of chiral Au NRs. (A) Calculated absorption, scattering, and extinction cross-sections of a colloidal distribution of chiral Au NRs under left- and right-handed excitation. (B) Calculated CD spectrum. The inset on the right shows the model of chiral Au NRs used for these calculations (length: 130 nm; diameter: 70 nm; wrinkle width: 3.5 nm).

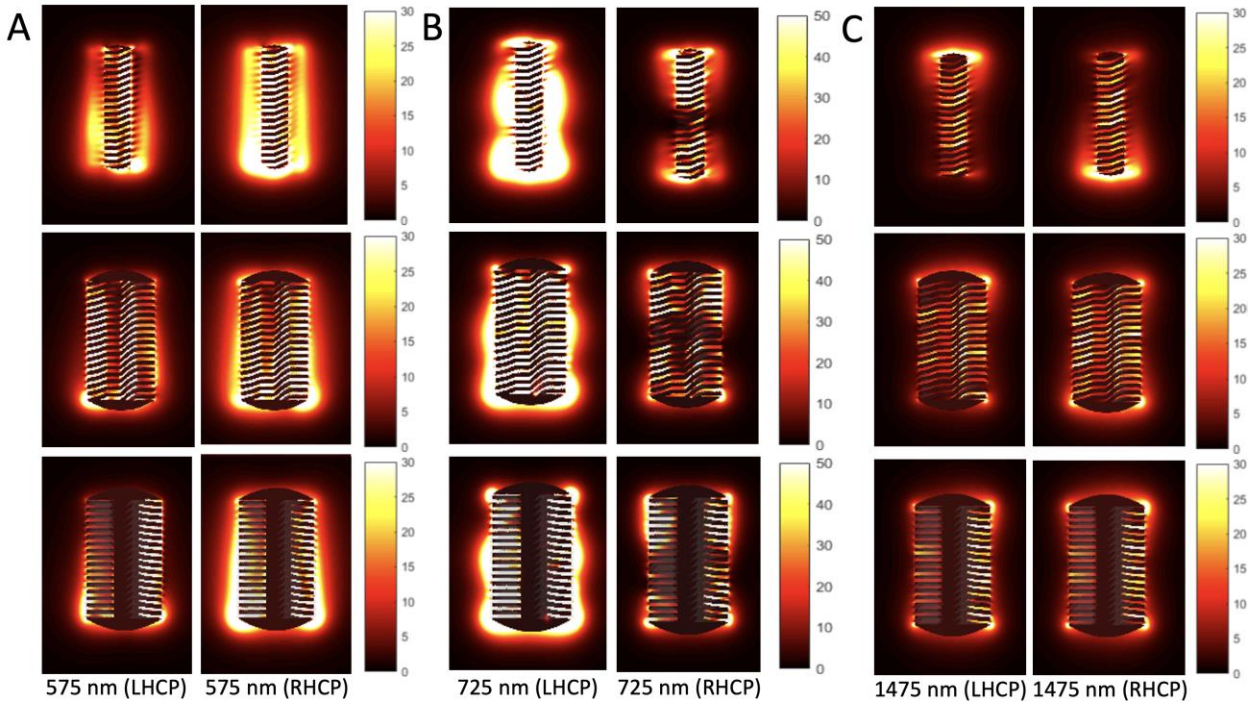

Figure 7. Simulated electric field enhancement profiles under left- and right-handed excitation for the chiral Au NR model shown in Figure 6, represented at different slices through the NR. (A) Calculated at 575 nm. (B) Calculated at 725 nm. (C) Calculated at 1475 nm. Illumination is from below, with a 10º inclination with respect to the Au NR axis. Note the different color scale in (B). Animated movies for each panel are provided as **Supplementary Movies S16-S17** (A), **S18-S19** (B), and **S20-S21** (C).

Conclusions

In summary, we have established a clear understanding of the morphological and spectral evolution during micelle-directed seed-mediated growth, from achiral to chiral Au NRs. A key turning point of the achiral-to-chiral transition has been found to be an intermediate elongated octahedral structure, which might be most efficient at accommodating helical micelle adsorption.

We additionally explored the roles of seed concentration, crystalline facets, and seed dimensions on the chiral overgrowth process, thereby providing a synthesis guide for tailored dimensions and optical activity. Moreover, we revealed an abnormally high absorption cross-section in wrinkled chiral Au NRs, which shows an exceptional size dependence, opposite to that of typical plasmonic nanoparticles. Last but not least, electromagnetic simulations allowed us to understand the high absorption and optical activity of chiral Au NRs, through simulated optical cross-sections and near-field profiles. These findings are of fundamental importance toward exploring the growth mechanism and optical properties of chiral plasmonic nanoparticles, as well as facilitating further application of chiral plasmonics.

METHODS:

Chemicals. Tetrachloroauric acid trihydrate ($HAuCl_4 \cdot 3H_2O$, ≥99%), sodium borohydride ($NaBH_4$, 99%), L-ascorbic acid (≥99%), silver nitrate ($AgNO_3$, ≥99%), hexadecyltrimethylammonium bromide (CTAB, ≥99%), *n*-decanol (98%), (*R*)-(+)-1,1'-binaphthyl-2,2'-diamine (*R*-BINAMINE, 99%), and (*S*)-(–)-1,1'-binaphthyl-2,2'-diamine (*S*-BINAMINE, 99%) were purchased from Sigma-Aldrich. Hexadecyltrimethylammonium chloride (CTAC, ≥99%) was purchased from ACROS. Hydrochloric acid solution (37 wt%) was purchased from Fisher Chemical. All chemicals were used without further purification. Milli-Q water (resistivity 18.2 MΩ·cm at 25 °C) was used in all experiments. All glassware was washed with aqua regia, rinsed with Milli-Q water, and dried prior to use.

Synthesis of Au NRs. Au NRs were prepared using a modified seeded growth method, using CTAB and *n*-decanol as binary surfactants according to a previous report.[28] Growth solutions A (CTAB 50 mM, *n*-decanol 13.5 mM) and B (CTAB 50 mM, *n*-decanol 11 mM) were prepared by

dissolving 9.111 g of CTAB together with 1.068 g and 870.5 mg of *n*-decanol in 500 mL of warm water, respectively. Both growth solutions were stirred at 50 °C for 1 h and then cooled down to room temperature. A typical synthesis involves three steps. First, for the synthesis of 1−2 nm Au seeds, a freshly prepared ascorbic acid solution (0.1 M, 0.025 mL) and a freshly prepared $NaBH_4$ solution (0.02 M, 0.2 mL) were successively added to a mixture composed of growth solution A (CTAB 50 mM, *n*-decanol 13.5 mM, 5 mL) and $HAuCl_4$ (0.05 M, 0.05 mL). The resulting seed solution was aged in a water bath at 25 °C for 30 min under mild stirring. Second, for the synthesis of small Au NRs (21 nm × 7.5 nm), the aged seed solution (0.6 mL) was injected into an aqueous solution containing growth solution A (CTAB 50 mM, *n*-decanol 13.5 mM, 10 mL), $HAuCl_4$ (0.05 M, 0.1 mL), $AgNO_3$ (0.01 M, 0.08 mL), HCl (1 M, 0.7 mL) and ascorbic acid (0.1 M, 0.13 mL), under vigorous stirring. The reaction solution was kept in a water bath at 25 °C for at least 4 h under stirring. The as-prepared small Au NR solution was centrifuged at 14000 rpm (~ 13000 g) for 45 min in 2 mL tubes. The precipitate was redispersed in CTAB solution (10 mM, 10 mL) and subjected to centrifugation under the same conditions, twice. For the growth of Au NRs (33 nm × 102 nm), the small Au NR solution (0.1 mL, OD_{400} = 9) was injected into an aqueous solution containing growth solution B (CTAB 50 mM, *n*-decanol 11 mM, 80 mL), $HAuCl_4$ (0.05 M, 0.8 mL), $AgNO_3$ (0.01 M, 1.6 mL), HCl (1 M, 3 mL) and ascorbic acid (0.1 M, 0.64 mL), under vigorous stirring. The reaction solution was kept in a water bath at 28 °C for more than 4 h under stirring. As-prepared Au NRs were centrifuged at 4000 rpm for 20 min twice and redispersed in water.

Synthesis of chiral Au NRs. Chiral NRs were prepared by a co-surfactant-assisted seeded growth, using single-crystalline Au NRs ([Au(0)] ~ 1 mM) as seeds.[14] Prior to the growth of chiral NRs, a co-surfactant solution was prepared by dissolving 24.9 mg of *S*-BINAMINE and 1.12 g of

CTAC in 35 mL of warm water at ~50 °C. The BINAMINE-CTAC solution was then cooled down to room temperature and stored in the dark. Single-crystalline Au NRs of different sizes were centrifuged (4000–9000 rpm, 15 min) and washed 3 times with CTAC solution (10 mM) and 2 more times with the BINAMINE-CTAC solution, followed by overnight incubation in the BINAMINE-CTAC solution at room temperature. The growth solution of chiral NRs was prepared by mixing 200 μL of the BINAMINE-CTAC solution, 600 μL of water, and 10 μL of $HAuCl_4$ solution (50 mM) in a 2 mL Eppendorf tube. After shaking and rest for 5 minutes, the growth solution color changed from pale yellow to brown, indicating the complexation of Au(III) with CTAC. Subsequently, 2–140 μL of the incubated single-crystalline Au NRs was quickly mixed with the growth solution, followed by a fast addition of 200 μL of L-ascorbic acid (0.8 M). The mixture was shaken vigorously and then kept undisturbed for 15 minutes, during which chiral NRs were formed. The solution was then centrifuged at 1500–4500 rpm for 10 min and redispersed in CTAC (1 mM).

NOTE: In all the steps mentioned above, using highly pure of CTAC (≥99%) was found crucial for the production of chiral Au NRs with high optical activity.

Characterization. TEM images were obtained on a JEOL JEM-1400PLUS TEM operating at an acceleration voltage of 120 kV. Elemental maps were performed on a JEOL JEM-2100F UHR TEM operating at an acceleration voltage of 200 kV and equipped with an Oxford INCA EDX system. HRSTEM and electron tomography experiments were performed using a "cubed" Thermo Fisher Scientific Themis Z electron microscope operated at 300 kV in HAADF-STEM mode. Tomography series were acquired over ±75° with tilt increments of 2°, reconstructions of tilt series were performed using the Astra Toolbox 1.8 for MATLAB 2018a.[40] Visualization of 3D reconstructions was performed using the Amira 5.4.0 software. Extinction, absorption, and

scattering spectra were measured using a UV/vis spectrophotometer Cary 5000 (Agilent Technologies Deutschland GmbH) equipped with an external diffuse reflectance accessory 2500 (integrating sphere). CD measurements were performed with a JASCO J-1500 CD spectrometer.

Electromagnetic modeling. The optical properties of chiral Au NRs were simulated using the M3 solver,[41–46] which implements a full-wave frequency-domain methodology based on boundary-element parametrizations (surface integral equation-method of moments, SIE-MoM). With this methodology, only the material boundaries (*i.e.*, two dimensional surfaces) must be parametrized, while no absorbing boundary conditions are required to close the problem, drastically reducing the size of the resulting algebraic problem, compared with conventional volumetric approaches. By applying Love's equivalence theorem, plasmonic nanorods can be substituted by equivalent surface electric and magnetic currents placed at the surface boundaries radiating in unbounded media, according to the Stratton-Chu expressions. The boundary conditions for the electric and magnetic fields are enforced in a variational sense with the help of functionals (specifically, we are applying the Galerkin formulation). This methodology offers great accuracy for solving unbounded scattering problems, particularly when dealing with resonant plasmonic response, as the singular behavior of fields is analytically handled by the Green's function and its derivatives. Gold was described through its dispersive complex permittivity, obtained from optical measurements.[47,48] All simulations were carried out on a workstation with two 256-core AMD EPYC 7H12 processors and 2 TB RAM.

ASSOCIATED CONTENT

Supporting Information. Additional results about the sample preparation, characterization, and simulations. Supporting Movies S1-S15: electron tomography reconstructions and related

orthoslices for selected Au NRs during chiral growth; Supporting Movies S16-S21: Simulated electric field enhancement profiles for a chiral Au NR, under different CPL, wavelength and orientation.

AUTHOR INFORMATION

Corresponding Authors

Xiaolu Zhuo: zhuoxiaolu@cuhk.edu.cn

Luis M. Liz-Marzán llizmarzan@cicbiomagune.es

Author Contributions

L.M.L.M. and X.Z. conceived the idea and wrote the manuscript. X.Z. carried out the synthesis, spectral characterization, and some structural characterization. M.M., W.H., and S.S. performed the electron tomography and electron diffraction. D.L., M.O.-L. and G.O.B carried out the numerical electromagnetic modeling. All authors participated in discussion of results and the preparation of the manuscript.

Notes

The authors declare no competing financial interest.

ACKNOWLEDGMENTS

This work has been supported by the European Research Council (ERC-AdG-4DbioSERS-787510 to L.M.L.-M. and ERC-CoG-REALNANO-815128 to S.B.) and the MCIN/AEI/10.13039/501100011033 (Grant PID2020-117779RB-I00). X.Z. acknowledges funding from Juan de la Cierva fellowship (FJC2018-036104-I) and University Development Fund (UDF01002665, CUHK-Shenzhen). D.L., M.O.-L. and J.M.T. acknowledge funding from the

European Regional Development Fund (ERDF) and the Spanish Ministerio de Ciencia, Innovación y Universidades, under Projects PID2020-116627RB-C21 and PID2020-116627RB-C22, as well as ERDF / Galician Regional Government as part of the agreement for funding the Atlantic Research Center for Information and Communication Technologies (atlanTTic) and ERDF / Extremadura Regional Government under Projects IB18073 and GR18055. This work was performed in the framework of the Maria de Maeztu Units of Excellence Program from the Spanish State Research Agency (Grant No. MDM-2017-0720). The authors acknowledge Dr. Guillermo González-Rubio for providing suggestions in synthesis, and Dr. Irantzu Llarena for assisting the CD measurements.

REFERENCES

1. Hentschel, M.; Schäferling, M.; Duan, X.; Giessen, H.; Liu, N. Chiral Plasmonics. *Sci. Adv.* **2017**, *3*, e1602735.

2. Kong, X. T.; Besteiro, L. V.; Wang, Z.; Govorov, A. O. Plasmonic Chirality and Circular Dichroism in Bioassembled and Nonbiological Systems: Theoretical Background and Recent Progress. *Adv. Mater.* **2020**, *32*, 1801790.

3. Li, L.; Shao, L.; Liu, X.; Gao, A.; Wang, H.; Zheng, B.; Hou, G.; Shehzad, K.; Yu, L.; Miao, F.; Shi, Y.; Xu, Y; Wang, X. Room-Temperature Valleytronic Transistor. *Nat. Nanotechnol.* **2020**, *15*, 743–749.

4. Li, W.; Coppens, Z. J.; Besteiro, L. V.; Wang, W.; Govorov, A. O.; Valentine, J. Circularly Polarized Light Detection with Hot Electrons in Chiral Plasmonic Metamaterials. *Nat. Commun.* **2015**, *6*, 8379.

5. Cai, J.; Zhang, W.; Xu, L.; Hao, C.; Ma, W.; Sun, M.; Wu, X.; Qin, X.; Colombari, F. M.; Farias de Moura, A.; Xu, J.; Silva, M. S.; Carneiro-Neto, E. B.; Gomes, W. R.; Vallée, R. A. L.; Pereira, E. C.; Liu, X.; Xu, C.; Klajn, R.; Kotov, N. A.; Kuang, H. Polarization-Sensitive Optoionic Membranes from Chiral Plasmonic Nanoparticles. *Nat. Nanotechnol.* **2022**, *17*, 408–416.

6. Tullius, R; Karimullah, A. S.; Rodier, M.; Fitzpatrick, B.; Gadegaard, N.; Barron, L. D.; Rotello, V. M.; Cooke, G.; Lapthorn, A.; Kadodwala, M. "Superchiral" Spectroscopy: Detection of Protein Higher Order Hierarchical Structure with Chiral Plasmonic Nanostructures. *J. Am. Chem. Soc.* **2015**, *137*, 8380–8383.

7. Kumar, J.; Eraña, H.; López-Martínez, E.; Claes, N.; Martín, V. F.; Solís, D. M.; Bals, S.; Cortajarena, A. L.; Castilla, J.; Liz-Marzán, L. M. Detection of Amyloid Fibrils in Parkinson's Disease Using Plasmonic Chirality. *Proc. Natl. Acad. Sci. U.S.A.* **2018**, *115*, 3225–3230.

8. Xu, L.; Wang, X.; Wang, W.; Sun, M.; Choi, W. J.; Kim, J. Y.; Hao, C.; Li, S.; Qu, A.; Lu, M.; Wu, X.; Colombari, F. M.; Gomes, W. R.; Blanco, A. L.; de Moura, A. F.; Guo, X.; Kuang, H.; Kotov, N. A.; Xu, C. Enantiomer-Dependent Immunological Response to Chiral Nanoparticles. *Nature* **2022**, *601*, 366–373.

9. Liu, T.; Besteiro, L. V.; Liedl, T.; Correa-Duarte, M. A.; Wang, Z.; Govorov, A. O. Chiral Plasmonic Nanocrystals for Generation of Hot Electrons: Toward Polarization-Sensitive Photochemistry. *Nano Lett.* **2019**, *19*, 1395–1407.

10. Liu, Z.; Ai, J.; Kumar, P.; You, E.; Zhou, X.; Liu, X.; Tian, Z.; Bouř, P.; Duan, Y.; Han, L.; Kotov, N. A.; Ding, S.; Che, S. Enantiomeric Discrimination by Surface-Enhanced

Raman Scattering–Chiral Anisotropy of Chiral Nanostructured Gold Films. *Angew. Chem. Int. Ed.* **2020**, *59*, 15226–15231.

11. Frank, B.; Yin, X.; Schäferling, M.; Zhao, J.; Hein, S. M.; Braun, P. V.; Giessen, H. Large-Area 3D Chiral Plasmonic Structures. *ACS Nano* **2013**, *7*, 6321–6329.

12. Zhang, M.; Pacheco-Peña, V.; Yu, Y.; Chen, W.; Greybush, N. J.; Stein, A.; Engheta, N.; Murray, C. B.; Kagan, C. R. Nanoimprinted Chiral Plasmonic Substrates with Three-Dimensional Nanostructures. *Nano Lett.* **2018**, *18*, 7389–7394.

13. Lee, H.-E.; Ahn, H.-Y.; Mun, J.; Lee, Y. Y.; Kim, M.; Cho, N. H.; Chang, K.; Kim, W. S.; Rho, J.; Nam, K. T. Amino-Acid-and Peptide-Directed Synthesis of Chiral Plasmonic Gold Nanoparticles. *Nature* **2018**, *556*, 360–365.

14. González-Rubio, G.; Mosquera, J.; Kumar, V.; Pedrazo-Tardajos, A.; Llombart, P.; Solís, D. M.; Lobato, I.; Noya, E. G.; Guerrero-Martínez, A.; Taboada, J. M.; Obelleiro, F.; MacDowell, L. G.; Bals, S.; Liz-Marzán, L. M. Micelle-Directed Chiral Seeded Growth on Anisotropic Gold Nanocrystals. *Science* **2020**, *368*, 1472–1477.

15. Urban, M. J.; Shen, C.; Kong, X. T.; Zhu, C.; Govorov, A. O.; Wang, Q.; Hentschel , M.; Liu, N. Chiral Plasmonic Nanostructures Enabled by Bottom-Up Approaches. *Annu. Rev. Phys. Chem.* **2019**, *70*, 275–299.

16. Zheng, G.; He, J.; Kumar, V.; Wang, S.; Pastoriza-Santos, I.; Pérez-Juste, J.; Liz-Marzán, L. M.; Wong, K. Y. Discrete Metal Nanoparticles with Plasmonic Chirality. *Chem. Soc. Rev.* **2021**, *50*, 3738–23754.

17. Xu, L.; Gao, Y.; Kuang, H.; Liz-Marzán, L. M.; Xu, C. MicroRNA-Directed Intracellular Self-Assembly of Chiral Nanorod Dimers. *Angew. Chem. Int. Ed.* **2018**, *57*, 10544–10548.

18. Zhou, C.; Duan, X.; Liu, N. DNA-Nanotechnology-Enabled Chiral Plasmonics: From Static to Dynamic. *Acc. Chem. Res.* **2017**, *50*, 2906–2914.

19. Lewandowski, W.; Vaupotič, N.; Pociecha, D.; Górecka, E.; Liz-Marzán, L. M. Chirality of Liquid Crystals Formed from Achiral Molecules Revealed by Resonant X-Ray Scattering. *Adv. Mater.* **2020**, *32*, 1905591.

20. Bagiński, M.; Tupikowska, M.; González-Rubio, G.; Wójcik, M.; Lewandowski, W. Shaping Liquid Crystals with Gold Nanoparticles: Helical Assemblies with Tunable and Hierarchical Structures *via* Thin-Film Cooperative Interactions. *Adv. Mater.* **2020**, *32*, 1904581.

21. Vila-Liarte D.; Kotov, N. A.; Liz-Marzán, L. M. Template-Assisted Self-Assembly of Achiral Plasmonic Nanoparticles into Chiral Structures. *Chem. Sci.* **2022**, *13*, 595–610.

22. Im, S. W.; Ahn, H.-Y.; Kim, R. M.; Cho, N. H.; Kim, H.; Lim, Y.-C.; Lee, H.-E.; Nam, K. T. Chiral Surface and Geometry of Metal Nanocrystals. *Adv. Mater.* **2020**, *32*, 1905758.

23. Lee, H. E.; Kim, R. M.; Ahn, H. Y.; Lee, Y. Y.; Byun, G. H.; Im, S. W.; Mun, J.; Rho, J.; Nam, K. T. Cysteine-Encoded Chirality Evolution in Plasmonic Rhombic Dodecahedral Gold Nanoparticles. *Nat. Commun.* **2020**, *11*, 263.

24. Kim, H.; Im, S. W.; Cho, N. H.; Seo, D. H.; Kim, R. M.; Lim, Y. C.; Lee, H. E.; Ahn, H. Y.; Nam, K. T. γ-Glutamylcysteine- and Cysteinylglycine-Directed Growth of Chiral Gold Nanoparticles and their Crystallographic Analysis. *Angew. Chem. Int. Ed.* **2020**, *59*, 12976–12983.

25. Cho, N. H.; Byun, G. H.; Lim, Y. C.; Im, S. W.; Kim, H.; Lee, H. E.; Ahn, H. Y.; Nam, K. T. Uniform Chiral Gap Synthesis for High Dissymmetry Factor in Single Plasmonic Gold Nanoparticle. *ACS Nano* **2020**, *14*, 3595–3602.

26. Kim, J. W.; Cho, N. H.; Lim, Y.-C.; Im, S. W.; Han, J. H; Nam, K. T. Controlling the Size and Circular Dichroism of Chiral Gold Helicoids. *Mater. Adv.* **2021**, *2*, 6988–6995.

27. Wang, W.; Zhao, J.; Hao, C.; Hu, S.; Chen, C.; Cao, Y.; Xu, Z.; Guo, J.; Xu, L.; Sun, M.; Xu, C. The Development of Chiral Nanoparticles to Target NK Cells and $CD8^+$ T Cells for Cancer Immunotherapy. *Adv. Mater.* **2022**, *34*, 2109354.

28. González-Rubio, G.; Kumar, V.; Llombart, P.; Díaz-Núñez, P.; Bladt, E.; Altantzis, T.; Bals, S.; Peña-Rodríguez, O.; Noya, E. G.; MacDowell, L. G.; Guerrero-Martínez, A.; Liz-Marzán, L. M. Disconnecting Symmetry Breaking from Seeded Growth for the Reproducible Synthesis of High Quality Gold Nanorods. *ACS Nano* **2019**, *13*, 4424–4435.

29. Goris, B.; Bals, S.; Van den Broek, W.; Carbó-Argibay, E.; Gómez-Graña, S.; Liz-Marzán, L.M.; Van Tendeloo, G.. Atomic-Scale Determination of Surface Facets in Gold Nanorods. *Nat. Mater.* **2012**, *11*, 930–935.

30. Barnard, A. S.; Curtiss, L. A. Modeling the Preferred Shape, Orientation and Aspect Ratio of Gold Nanorods. *J. Mater. Chem.* **2007**, *17*, 3315–3323.

31. Zhang, Q.; Han, L.; Jing, H.; Blom, D. A.; Lin, Y.; Xin, H. L.; Wang, H. Facet Control of Gold Nanorods. *ACS Nano* **2016**, *10*, 2960–2974.

32. Wang, Q.; Wang, Z.; Li, Z.; Xiao, J.; Shan, H.; Fang, Z.; Qi, L. Controlled Growth and Shape-Directed Self-Assembly of Gold Nanoarrows. *Sci. Adv.* **2017**, *3*, e1701183.

33. Heyvaert, W.; Pedrazo-Tardajos, A.; Kadu, A.; Claes, N.; González-Rubio, G.; Liz-Marzán, L. M.; Albrecht, W.; Bals, S. Quantification of the Helical Morphology of Chiral Gold Nanorods. *ACS Materials Lett.* **2022**, *4*, 642–649.

34. Sun, L.; Zhang, Q.; Li, G. G.; Villarreal, E.; Fu, X.; Wang, H. Multifaceted Gold–Palladium Bimetallic Nanorods and their Geometric, Compositional, and Catalytic Tunabilities. *ACS Nano* **2017**, *11*, 3213–3228.

35. Jenkinson, K.; Liz-Marzán, L. M.; Bals, S. Multimode Electron Tomography Sheds Light on Synthesis, Structure, and Properties of Complex Metal-Based Nanoparticles. *Adv. Mater.* **2022**, 2110394.

36. Jimenez de Aberasturi, D.; Serrano-Montes, A. B.; Liz-Marzán, L. M. Modern Applications of Plasmonic Nanoparticles: From Energy to Health. *Adv. Opt. Mater.* **2015**, *3*, 602–617.

37. Höller, R. P.; Dulle, M.; Thomä, S.; Mayer, M.; Steiner, A. M.; Förster, S.; Fery, A.; Kuttner, C.; Chanana, M. Protein-Assisted Assembly of Modular 3D Plasmonic

Raspberry-Like Core/Satellite Nanoclusters: Correlation of Structure and Optical Properties. *ACS Nano* **2016**, *10*, 5740–5750.

38. Maier, S. A. *Plasmonics: Fundamentals and Applications.* Springer: New York, 2007.

39. Yu, R.; Liz-Marzán, L. M.; García de Abajo, F. J. Universal Analytical Modeling of Plasmonic Nanoparticles. *Chem. Soc. Rev.* **2017**, *46*, 6710–6724.

40. Van Aarle, W.; Palenstijn, W. J.; De Beenhouwer, J.; Altantzis, T.; Bals, S., Batenburg, K. J.; Sijbers, J. The ASTRA Toolbox: A Platform for Advanced Algorithm Development in Electron Tomography. *Ultramicroscopy* **2015**, *157*, 35–47.

41. Solís, D. M.; Taboada, J. M.; Obelleiro, F.; Liz-Marzán, L. M.; García de Abajo, F. J. Toward Ultimate Nanoplasmonics Modeling. *ACS Nano* **2014**, *8*, 7559–7570.

42. Solís, D. M.; Taboada, J. M.; Obelleiro, F.; Liz-Marzán, L. M.; García de Abajo, F. J. Optimization of Nanoparticle-Based SERS Substrates through Large-Scale Realistic Simulations. *ACS Photonics* **2017**, *4*, 329–337.

43. Taboada, J. M.; Rivero, J.; Obelleiro, F.; Araújo, M. G.; Landesa, L. Method-of-Moments Formulation for the Analysis of Plasmonic Nano-Optical Antennas. *J. Opt. Soc. Am. A* **2011**, *28*, 1341–1348.

44. Taboada, J. M.; Araujo, M. G.; Obelleiro Basteiro, F.; Rodriguez, J. L.; Landesa, L. MLFMA-FFT Parallel Algorithm for the Solution of Extremely Large Problems. *Electromagn. Proc. IEEE* **2013**, *101*, 350–363.

45. Solís, D. M.; Taboada, J. M.; Obelleiro, F.; Surface Integral Equation-Method of Moments with Multiregion Basis Functions Applied to Plasmonics. *IEEE Trans. Antennas Propag.* **2015**, *63*, 2141–2152.

46. Martín, V. F.; Landesa, L.; Obelleiro, F.; Taboada, J. M. A Discontinuous Galerkin Vombined Field Integral Equation Formulation for Electromagnetic Modeling of Piecewise Homogeneous Objects of Arbitrary Shape. *IEEE Trans. Antennas Propag.* **2022**, *70*, 487–498.

47. Johnson, P. B.; Christy, R. W. Optical Constants of the Noble Metals. *Phys. Rev. B* **1972**, *6*, 4370–4379.

48. Palik, E. D. *Handbook of Optical Constants of Solids.* Academic Press: San Diego, 1985.

Table of Contents (TOC) Graphic